In-situ deposition of three-dimensional graphene on selective laser melted copper scaffolds for high performance applications

Kaka Cheng[a], Wei Xiong[a], Yan Li[a,b,*], Liang Hao[a,b], Chunze Yan[c], Zhaoqing Li[c], Zhufeng Liu[c], Yushen Wang[a], Khamis Essa[d], Li Lee[e], Xin Gong[e], Ton Peijs[f]

[a] Gemmological Institute, China University of Geosciences, Wuhan 430074, PR China
[b] Hubei Gem and Jewelry Engineering Technology Research Center, Wuhan 430074, PR China
[c] School of Materials Science and Engineering, Huazhong University of Science and Technology, Wuhan 430074, PR China
[d] Mechanical Engineering, University of Birmingham, Birmingham B15 2TT, UK
[e] School of Electrical and Electronic Engineering, Huazhong University of Science and Technology, Wuhan 430074, PR China
[f] WMG, Materials Engineering Centre, University of Warwick, CV4 7AL Coventry, UK

ARTICLE INFO

ABSTRACT

Currently, three-dimensional graphene (3DG) fabrication was restricted by the complicated process, strict chemical reactions as well as structural accuracy. Herein we creatively propose a bottom-up strategy that leverages the selective laser melting (SLM) technique to manufacture a three-dimensional (3D) porous copper template. Graphene was then in-situ grown via chemical vapor deposition (CVD) on the obtained porous Cu template, forming 3DG composites. A combination of conventional graphene growth via CVD technique with SLM fabricated scaffold templates enabled an accurate design and regulation of 3DG from macro-structure (unit type, porosity, aperture) to micro-structure (texture, surface quality) through an elaborately manipulated porous copper scaffold. The 3DG/copper scaffold could achieve around 88% and 27% enhancement in electromagnetic interference (EMI) shielding and thermal diffusion, respectively. Particularly, the highest EMI shielding efficiency (SE) can reach up to 47.8 dB at 2.7 GHz and exhibit an average SE of 32.3 dB at the range of 2–18 GHz. The synergistic shielding mechanisms accounted for the improvement derived from the use of hybrid composite materials and precise architecture of the SLM porous structure.

1. Introduction

Graphene, consisting of sp^2 hybridized carbon atoms, has gained wide popularity owing to its advantageous performance, such as high surface area (2630 m^2 g^{-1}) [1], excellent intrinsic carrier mobility (2 × 10^5 cm^2 V^{-1} s^{-1}) and superior thermal conductivity (~5000 W m^{-1} K^{-1}) [2]. However, the strong π-π interaction between two dimensional (2D) single-layer graphene sheet is prone to aggregation, because graphene suffers from shape instability as it tends to roll, scroll, wrinkle, fold - up unless it is constrained onto a solid surface [3]. Aforementioned features lead to significantly reduced effective properties and a gap between theoretical promises and practical applications. Confronting with these problems, three-dimensional graphene (3DG) shows better promise in high porosity (~99.7%), low specific gravity (~0.6 mg m^{-2}) [4] accompanied with higher specific surface areas as well as loading capacity, faster electronic conduction and mass transfer even superior to that of two-dimensional graphene

(2DG), extending applications in catalysis [5], energy storage [6,7], sensors [4], electromagnetic interference (EMI) shielding [8] and so on.

Various types of methods regarding 3DG preparation have been developed, including freeze drying [9], hydrothermal reaction [10], self-assembly [11], de-alloy [12] and so on. However, the aforementioned methods are still facing some challenges. For example, freeze drying and hydrothermal reaction suffer from poor control on morphologies and connections of graphene layers [13]. Self-assembly method requires long process time (several days) owing to dialysis and lyophilization [14]. De-alloy method shows limitation on controlling the types and quantities of pores due to the selective dissolution of composition [15]. Most approaches mentioned above are hardly to construct desirable structure to satisfy the requirement of functional design, while template-directed CVD method shows this superiority, as well as the advantages of large-area and high-quality graphene [16]. By this method, when temperature is cooling down, carbon is soluble and the graphene form on the metal substrate which acts as a reaction

---

catalyst. The microscopic characteristics (i.e., composition and microstructure), exert a determined influence on the final microstructure (i.e., layer thickness, defects) of the prepared 3DG. Besides, the generated 3DG will inherit the macro properties from the metal template (i.e., porosity, pore size, surface quality). However, most of the porous metal templates prepared by conventional methods have difficulty preciously regulating porosity, for instance, the commercial Ni foam generally changes the porosity by roughly controlled foaming agent content, the subsequently obtained 3DG shows poor control of macroscopic and microscopic features for specific functional design [17,18]. Hence, it is of necessity to develop metal templates, which can be precisely manipulated from macro to micro aspects to achieve 3DG with tunable structures and stable performances [19].

Selective laser melting (SLM), as an innovative additive manufacturing (AM) technology, is particularly designed for the fabrication of sophisticated and/or precise three-dimensional (3D) metal templates with great advantages of complexity in design, efficiency in production and flexibility of *in-situ* manufacturing capability. To date, numerous researches have reported SLM porous structures of Ti alloys [20], stainless alloys [21], and Ni alloys [22]. Cu is the most widely used foil/substrate for large-area graphene synthesized in state-of-the-art research and industrial areas. Compared with Ni or other substrate, copper is regarded as a more desirable substrate for graphene growth via CVD due to the lower carbon saturation level (< 0.001 at. %) and growth process self-limiting of copper, which tend to generate high-quality single layered graphene with larger areas [23]. While Ni has a higher carbon solubility (> 0.1 at. %) [17], thick graphene films tend to form because of excessive carbon precipitation [24]. However, research in SLM of pure copper is still in its infancy because of insufficient heating for powders melting derived from its intrinsic high thermal conductivity and reflectivity towards common laser wavelength (1000–1100 nm). Fabrication of precise and condense copper scaffolds via SLM is still facing many challenges [25].

To overcome above limitations, we here for the first time propose a feasible bottom-up approach to produce 3DG/copper (3DG/Cu) structures via SLM simultaneously in combination with CVD growth of graphene. A well-designed gyroid-type porous copper template was initially investigated via SLM from microstructural evolution to macroscopic performance, especially with respect to anisotropy and heterogeneity. Then *in-situ* graphene growth on this porous copper template via CVD method resulted in the 3DG/Cu structure. By combining excellent electrical (5.7×10^7 S m^{-1}) and thermal conductivities (398 W m^{-1} K^{-1}) with the good mechanical properties of copper, 3DG/Cu not only presents excellent functionalities in the electrical and thermal field, but also displays lightweight and robust design, preventing 3DG from collapsing with the aid of the metal template. The synergistic effects from multi-materials and porous structures enable great improvements in EMI and thermal management performance of the lightweight 3DG/Cu scaffold. Specifically, the 3DG/Cu composite structure displays a multiple shielding mechanism network with strong microwave attenuation from reflection and absorption shielding efficiency (*SE*). The regulation of the SLM porous template via precise design of architectures for optimized properties is comprehensively discussed in this work.

2. Experimental

2.1. Materials

The pure gas atomized copper powder was micron-size and most of the particles exhibit a spherical shape, which can increase the fluidity and packing density compared to polyhedral ones [26]. The average particle size was 18.856 $\pm$ 15 μm, smaller than the laser spot (30 μm) (Fig. S1). The chemical composition of the initial copper powder is listed in Table S1.

2.2. Preparation of Cu components via SLM

To approach quality copper samples, a thorough parameter investigation from single line to cubic formation was conducted using a SISMA MYSINT100 system with an Nd:YAG fiber laser (wavelength of 1060 nm, maximum output laser power of 200 W, laser spot size of 30 μm) under high purity nitrogen gas atmosphere (residual oxygen concentration < 0.5 vol.%), protecting the powder from oxidation. It is worthy of knowing that the used laser spot is much smaller than the common laser (100 μm), which can ensure the fine architectures.

Samples of rectangular contour (1.0 × 2.5 mm) and cubic samples (8 × 8 × 8 mm^3) were fabricated for single track and bulk experience, respectively. The processing parameters window for the cubic samples (Table S2) and the laser scanning strategy was chessboard with each layer divided into four squares, and with the scanning direction inside the square perpendicular to that of the adjacent square. Based on preliminary research, the laser power and layer thickness were fixed at 180 W and 0.02 mm to ensure formability. Different volumetric laser energy densities are investigated (Eq. (1)).

$$E = \frac{P}{v \times h \times t} \tag{1}$$

Where *E*, *P*, *v*, *h* and *t* represent the volumetric laser energy density (J/mm^3), laser power (W), scanning speed (mm/s), hatch distance (mm) and layer thickness (mm), respectively.

Specific size samples with different orientations (parallel to the x- and z-axis) labeled as EC-x, EC-z (2 × 2 × 20 mm^3), TC-x, TC-z (2 × 10 × 10 mm^3) were for electrical and thermal conductivities test according to ASTM B193-2002 and ASTM E1461-2013, respectively. The Gyroid-type porous cylinder specimens ($\Phi = 7 \times 3.05 \times 2$ mm) were fabricated under the optimal processing parameters for cubic samples according to ASTM ES7-83 (Table S2). Based on previous study, 26 PPI and 17 PPI scaffolds were prepared, with pore radius of 250 μm and 450 μm, respectively.

2.3. Synthesis of 3DG/Cu porous scaffold via CVD

3DG/Cu scaffolds were manufactured using the following procedures (Fig. 1). The SLM copper scaffold template was placed into the quartz tube of the CVD system (G-CVD-5, China). The CVD process can be found in previous report [24]. For comparison, a group of copper scaffolds processed heat treatment (HT) under the same temperature (For more details please refer to Supporting Information Table S3).

2.4. Characterization techniques

The starting powder was characterized by inductively coupled plasma-mass spectrometry (ICP-Ms, Agilent 7700, US). The size distribution of the powder was analyzed by a particle size analyzer (Runzhi Rise-2002, China). The surface morphology and microstructure were observed under an optical microscopy (OM, Leica A205, Germany) and scanning electron microscope with an energy dispersive spectroscopy (SEM-EDS, Hitachi-Su8010, Japan). Before metallographic observation, the rectangular contour samples were processed polishing and etchant (in a mixed solution of 5 g FeCl$_3$, 5 ml HCl and 100 ml distilled H$_2$O for 10 s) according to a standard metallographic procedure. The density of the cubic samples was measured by the Archimedes method and presented as a relative density to the copper powder (8.9 g/cm^3). Phase structure was tested using X-ray diffraction (XRD, Bruker D8 Advance, Germany) with Cu-Kα radiation at 40 KV and 40 mA in the range 2θ = 20°–90°, using a step size of 0.02°. The Vickers hardness measurements were carried out on both horizontal and vertical planes of the specimens at a load of 3 N (HV3) and a dwell time of 10 sec. Ten indentations points were conducted from one edge to the opposite across the surface of the samples and average values were reported. The electrical resistivity measurement (ZEM-3) met
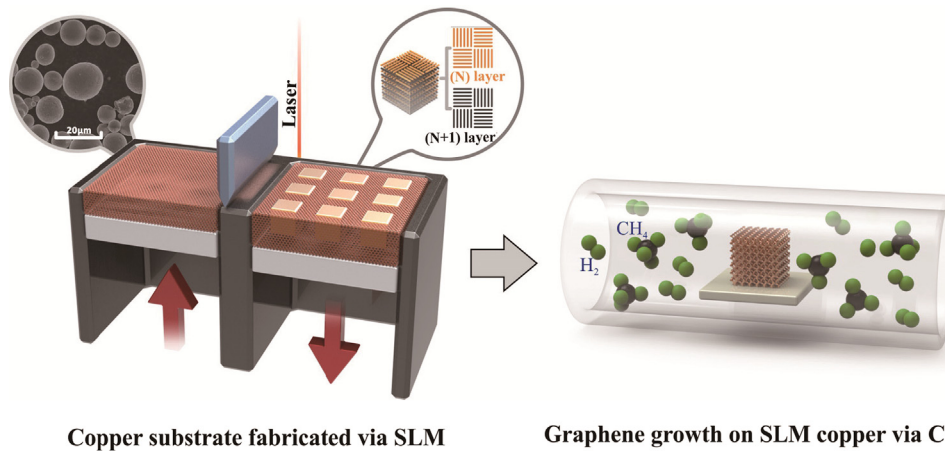
Fig. 1. Illustration of the 3DG/Cu porous structure fabrication process: copper scaffold fabricated via SLM (left) and *in-situ* graphene growth on the copper scaffold via CVD (right). (For interpretation of the references to colour in this figure legend, the reader is referred to the web version of this article.)

ASTMB193-2002 requirements with a sample size of $2 \times 2 \times 20$ mm^3 from both horizontal and vertical orientations. The thermal diffusivity measurement on the cubic ($2 \times 10 \times 10$ mm^3) and porous structure ($5 \times 10 \times 10$ mm^3) followed ASTME1461-2013 with a sample size of the aforementioned two orientations using the LFA (Laser flash method, Netzsch LFA457, Germany). Raman spectroscopy (SENTERRA, Bruker, Germany) was used to characterize the 3DG/Cu scaffold with an excitation wavelength of 514 nm. The S parameters ($S11$ and $S21$) were measured with a vector network analyzer (VNA, Agilent PNA-N5244A, US) using the coaxial method in 2–18 GHz. The values of SE_{total}, SE absorption, and SE reflection were determined as Eq. 2–5 in the Supporting Information.

3. Results and discussion

3.1. Formation of SLM copper

3.1.1. SLM manufacturing of copper under different line energy densities

The most effective parameters (laser power and scanning speed) were preliminarily investigated via single track experience. Different types of single tracks were observed and the processing window could be divided into four distinguishing zones (Fig. 2) based on the melting tracks quality, including 30% weak sintering zone (A), 26.7% unstable melting zone (B), 16.7% continuous track zone (C) and 26.7% excessive melting zone (D). Different zones represent diverse line energy density, LED (J/m) [27] (Eq. 6, please refer to SI). The selected laser device and processing optimization proved to overcome the challenges of high reflectivity and thermal conductivity of copper. The less continuous track area also indicated the forming difficulty with limited process parameters. In zone A, scanning track was difficult to form because the line energy density was insufficient. In zone B, the powder could not form stable width tracks with lots of unmolten powder sticking to the surface owing to energy deficiency. The melt flow of the molten pool becomes stable with sufficient depth of penetration into the former layer and as a result, a relatively smooth track was obtained with a minimum input LED of 400 J/m (zone C). When an excessive LED (> 800 J/m) is applied, a roughly 130 μm wide track occurred and micro-cracks also appeared (zone D), which were caused by high residual stresses resulting from the excess heat accumulation associated with the high power as well as low scanning speed [28].
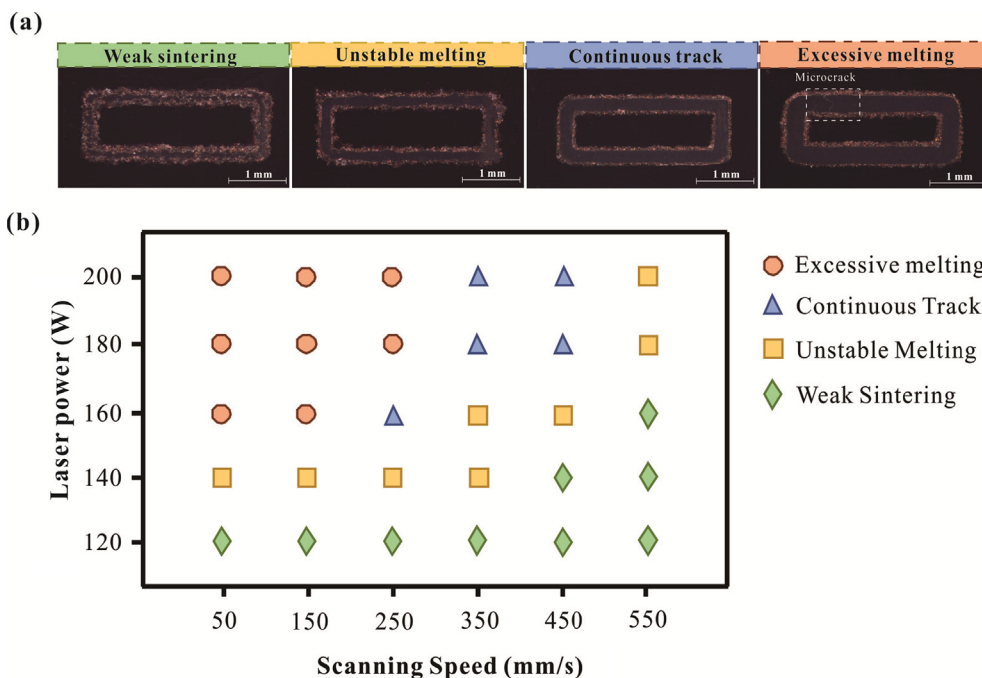

Fig. 2. (a) Typical track types of a weak sintering zone, unstable melting zone, continuous track zone, and excessive melting zone, respectively; (b) processing window of laser power and scanning speed. (For interpretation of the references to colour in this figure legend, the reader is referred to the web version of this article.)
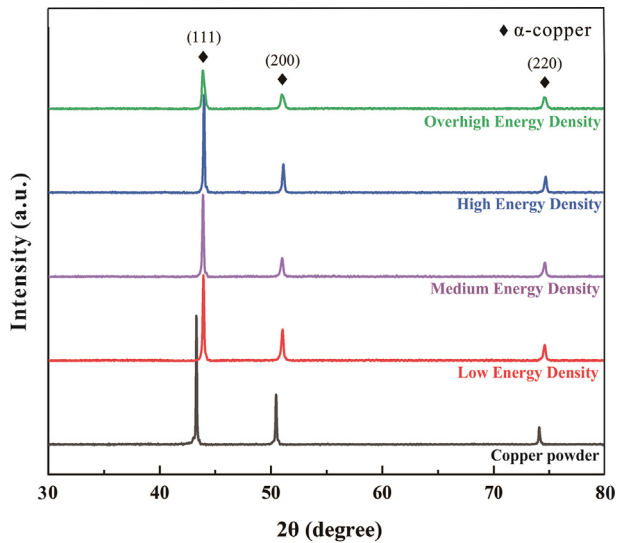
Fig. 3. XRD patterns of the starting copper powder and as-built copper specimens. (For interpretation of the references to colour in this figure legend, the reader is referred to the web version of this article.)

3.1.2. Formation of anisotropic microstructure under different volumetric energy density

The main phase α-copper could be clearly characterized in all XRD patterns by the (1 1 1) and (2 0 0) reflections diffracted at 2θ = 43.32° and 2θ = 50.45°, respectively (Fig. 3), and the (1 1 1) direction was much prevailing. The as-built copper specimens presented similar XRD patterns to the starting powder and the distinguishing differences in the broadening breadth of peaks which implied grain refinement in the SLM process. In addition, the diffraction peaks of SLM samples shifted to higher diffraction angles, indicating an enhancement of residual stress in the as-built samples due to the high cooling rate [29].

The morphology of the molten pool was characterized on the vertical section of the SLM pure copper part to analyze defect mechanisms of samples with varying energy input. Three main types of defects were observed: (i) inter-layer voids, (ii) non-melted powder, and (iii) gas pores. At excessive input energy of 3000 J/mm^3 (Fig. 4a), the melt pool was as wide as 180 μm, six times wider than for the low energy one (Fig. 4d). The droplet spatters could be seen due to the Marangoni convection [30] causing dramatic fluctuation and evaporation in the molten pool. These spatters later became inter-layer inclusions which hindered the powder spreading processing and finally leading to voids inside the part. With the input energy further decreasing and settling at 857 J/mm^3, sound parts with few microspores were obtained and the molten pool size diminished as indicated by the yellow dash (Fig. 4b). Under these conditions, the pure copper part achieved highly densification up to 96.2% with good metallurgical bonding. However, with decreasing input energy by enhancing the hatch distance, irregular pores and non-melted area were dispersed in the neighboring layers. The heat in the molten pool transmitted fast to the surrounding area due to the high thermal conductivity of pure copper (398 W m^{-1} K^{-1}), and thus insufficient input energy was unable to melt the raw materials thoroughly (Fig. 4c). Gas holes could also be found in this case, which failed to escape from the molten pool and were trapped by the Marangoni convection. Besides, the detected phosphorous content in the raw materials may also lead to gas holes and the oxides may act as nucleation sites for pore formation during the SLM process [31]. In contrast, at lower input energy of 128 J/mm^3, pockets of non-melted powder and irregular voids appeared across the whole sample with narrow-shallow fish scale-like voids, accounting for 88.6% of the relative density (Fig. 4d).

The evolution of microstructures in the SLM process were shown to understand the relevant changes (Fig. 5). The typical epitaxial columnar grains parallel the building direction were formed on the vertical section, which were mainly attributed to the anisotropy feature derived from the temperature gradient. The temperature gradient vector at the solid–liquid interface is from the center of the molten pool to the bottom owing to the vertically downwards heat conduction path to the substrate, which facilitates the growth of columnar microstructures [32]. The extremely high thermal conductivity of pure copper in solid state intensifies the heat flow along the building direction. Similar to the work by Wang et al. [33], the equiaxed cell became the dominant structure in the horizontal plane, resulting from
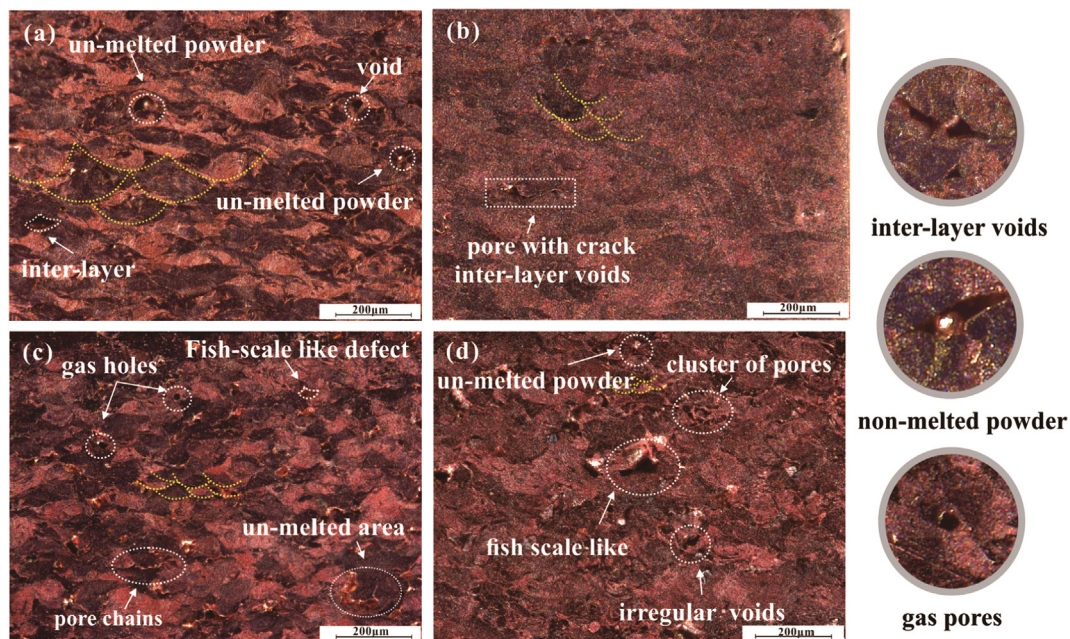

Fig. 4. Optical micrographs of typical morphology of samples fabricated by various input energy in vertical direction: (a) excessive (3000 J/mm^3), (b) high (857 J/mm^3), (c) medium (285 J/mm^3), (d) low energy (128 J/mm^3), respectively. (For interpretation of the references to colour in this figure legend, the reader is referred to the web version of this article.)
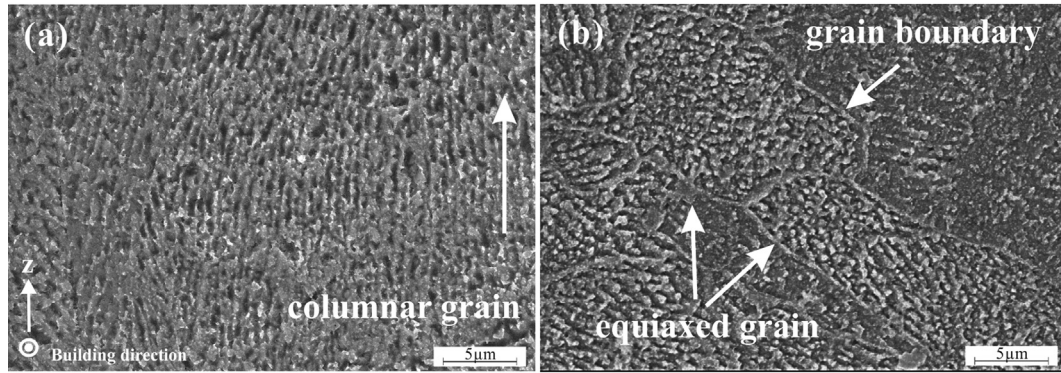
Fig. 5. SEM images of typical microstructures on the etched vertical and horizontal planes of as-built parts.

heat radiation through the surrounding powder bed and environment. The average grain size in the horizontal section of the copper SLM samples was < 100 μm, much finer than that of casted reference samples (400 μm), corresponding to the significantly different cooling rate between the SLM samples (10^5–10^8 K/s) and the cast samples (1 K/s) [34].

3.2. Effect of anisotropic microstructure on properties of SLM copper

3.2.1. Effect of anisotropic microstructure on Vickers microhardness

A Vickers hardness profiles in Fig. 6 is used to assess the possible effect of different energy densities and orientations on microhardness. The average Vickers hardness initially increased to the peak value of 92.9 HV at 857 J/mm^3 and then decreased with reduced input energy. The excessive energy led to coarser grains as well as more serious spattering behavior, which were both attributed to the lower hardness [35]. Correspondingly, at low input energy (128 J/mm^3), macroscopic defects extremely deteriorated the hardness performance according to low relative porosity. The hardness value of the vertical section was 6.3% higher than that of the horizontal one. Two reasons may well account for this phenomenon. Firstly, the anisotropic grain morphology was illustrated in Fig. 5. Secondly, the tested horizontal section referring to the top region of the SLM parts experienced much more heat loss by convection and radiation but less thermal re-melting than the prior layers. A heterogeneity in hardness was also observed on the vertical
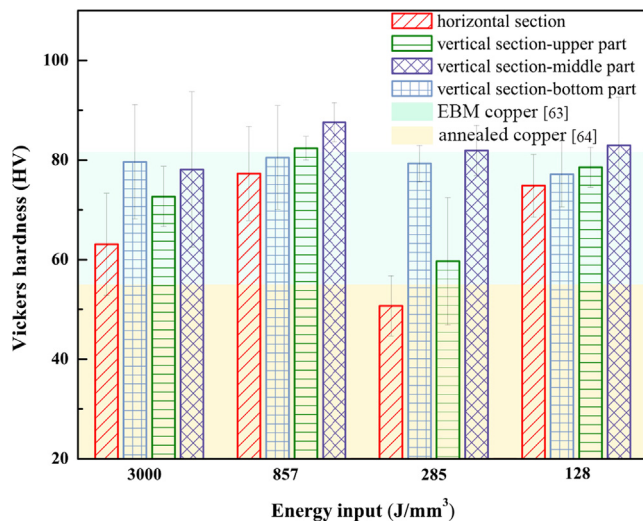
section, that the middle region almost surpassed other regions because of enough thermal cycling.

The highest hardness value of the SLM-built copper specimens achieved in this work has a substantial increase of nearly 68.9% and 5.6% compared with annealed pure copper (55 HV) and electron beam melting (EBM) prepared ones (88 HV) [36]. The ultrafine microstructure derived from rapid solidification during the SLM process accounts for the superior hardness.

3.2.2. Effect of anisotropic microstructure on electrical and thermal conductivities

The electrical conductivity of as-built samples (Fig. 7a), from both x- and z-axis orientations increased with the enhancing input energy density and was in proportional to the density. The electrical conductivity was up to 3.1 × 10^{-1} S/m at a maximum volume energy density of 3000 J/mm^3, which was equivalent to 53.8% International Annealed Copper Standard (IACS, the definition of 5.8 × 10^{-1} S/m as 100% IACS for electrical conductivity). During the SLM process, the dense grain boundaries derived from the high cooling rate impede the electron movement, which may partly explain the inferior electrical conductivity compared with that of conventional methods. With an input energy above 857 J/mm^3, the electrical conductivity of EC-z samples showed superior behavior, coinciding with the epitaxial columnar grains aligned parallel to the build direction (similar to the test electron transmit direction). Such columnar grains attributed to fewer grain boundaries and the vast electrons transported with less scattering, leading to higher electrical conductivity and vice versa along the horizontal one [37]. For input energy below 857 J/mm^3, the electrical conductivity exhibited an opposite trend because lower density caused severer side-effects (defects and non-melted powder).

Similar to the electrical conductivity, an obvious difference in thermal conductivity was observed for diverse measurement orientations (Fig. 7b). For high-density samples (> 285 mm^3/J), the thermal conductivity of TC-x samples gradually increased to 214.7 W m^{-1}K^{-1}, while the TC-z samples were opposite. During the SLM process, the molten pool size reduced with decreasing input energy and grain growth inclined to follow the radial direction of maximum heat flux, according to the competitive growth mechanism [38]. As a result, grains grew nearly parallel to the x-axis (equal to the test heat flow direction) as the molten pool became narrower and shallower with a decreasing input energy (Fig. 7c, e). This was beneficial to the thermal conductivity because conductive pathways for electron and phonon transport along the direction of the aligned grains (Fig. 7d). However, at the low-density range (< 285 mm^3/J), both groups exhibited lower conductivity due to defect barriers. Because the primary mechanisms of electrical and thermal conductivities are the movement of free electrons, the experimental value of thermal conductivity was compared with theoretical values to verify Wiedemann–Franz law (Eq. 7 in Supporting Information). A good fit was observed (Fig. 7b), while little

Fig. 6. Vickers hardness of SLM-built samples among various input energies compared with EBM [63] and anneal copper [64]. (For interpretation of the references to colour in this figure legend, the reader is referred to the web version of this article.)
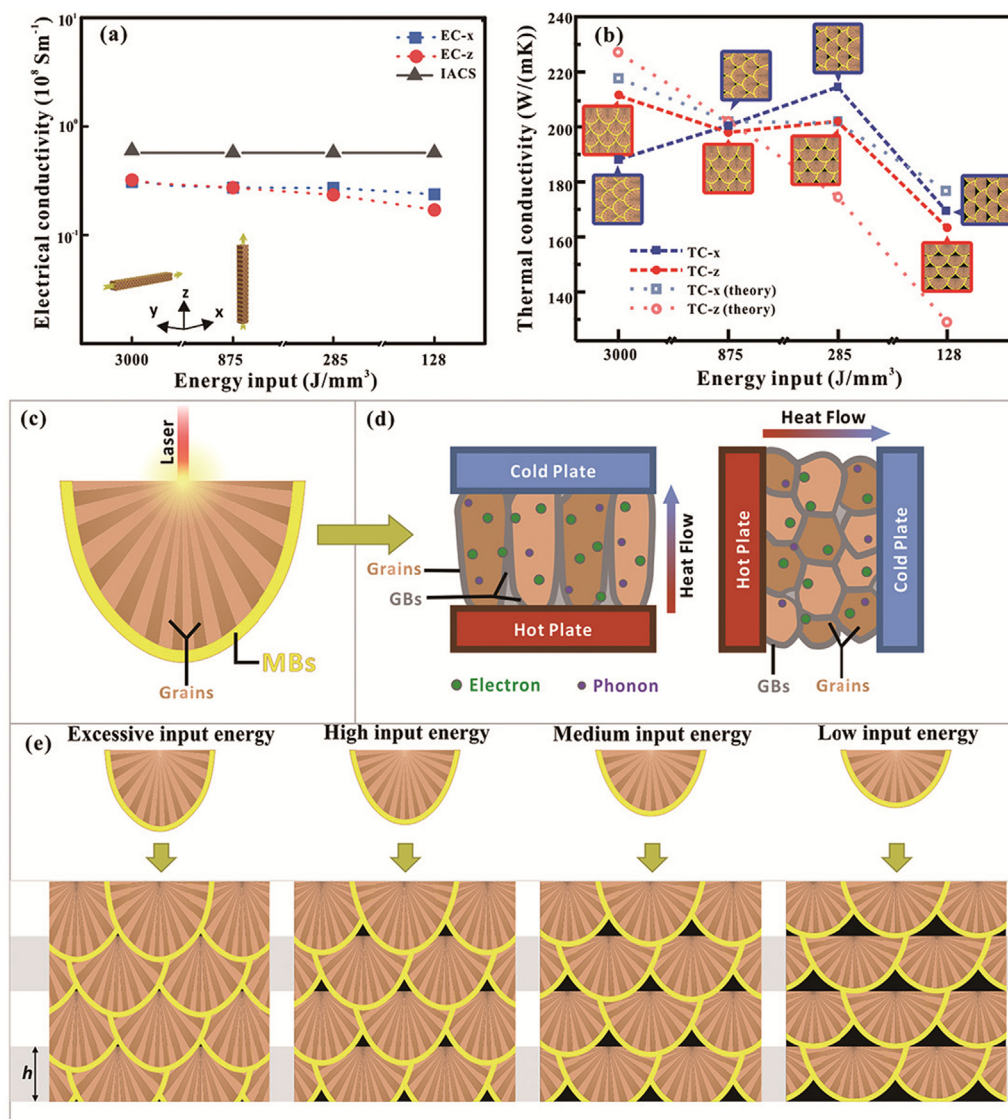
Fig. 7. (a) Electrical and (b) thermal conductivity for four types of input energy; (c) schematic of molten pool; (d) schematic of thermal conductivity measurement; (e) schematic of molten pool formation under different input energy. (Error bars are omitted for better reading). (For interpretation of the references to colour in this figure legend, the reader is referred to the web version of this article.)

discrepancy derived from sample size and microstructure.

3.3. Morphology and structure of CVD 3DG/Cu porous scaffolds

Fine prepared copper porous scaffolds with different porosity were manufactured using optimal processing parameters to leverage the anisotropy in aforementioned performance effectively. Graphene was then *in-situ* grown on the copper template via CVD method. As the growth of graphene on the copper substrate mainly involves surface diffusion and nucleation of carbon atoms, obeying a surface adsorption mechanism, the interaction between copper catalyst and graphene film is relatively feeble [39]. According to density functional theory, graphene has weak bonding with copper substrate at a low binding energy of 33 meV per carbon atom, similar to the interplanar binding of graphite (25 meV per carbon atom) [39]. Using carbon isotope labeling during graphene growth on Cu and Ni, Li et al. [40] demonstrated that no metal-carbide compound formed during the growing process. However, considerable advances in chemical transfer methods (e.g. direct transfer method [23], polymer-free transfer methods [41]) were developed to remove the CVD-grown graphene from the substrate, reflecting that there was enough interaction between the graphene and metal. Actually, we have tried to investigate the interface of graphene and metal substrate using SEM, which gave the cross-section morphology not the exact value of interaction force. The SEM microstructure of the prepared 3DG/Cu porous scaffold revealed good metallurgical bonding of copper powder with a strut diameter of approximately 450 μm (Fig. 8**a**). According to high magnification images of the morphology (Fig. 8**b**), graphene flakes were obvious near the fringe of the scaffold, especially in the defect region. To demonstrate the distribution of graphene on the scaffold substrate, EDS mapping indicated the successful growth of graphene on the copper cellular template with nearly uniform distribution (Fig. 8**c-d**), which confirmed the potential of parameter adjustment in substrate fabrication. A graphene flake was particularly detected at higher magnification (Fig. 8**e-g**). The obtained 3DG/Cu porous hybrid scaffold showed relatively weak luster compared with the initial counterpart (Fig. 8**h**).

Raman spectroscopy was further performed on the 3DG/Cu to obtain additional structural information. The typical G-band (~ 1590 cm^{-1}) as well as the 2D-band (~2699 cm^{-1}) suggested a narrow thickness distribution around mono to few layers [42] (Fig. 8i). Since the D-band (~ 1350 cm^{-1}) reflects the disordered carbon level in graphene [43], the intensity ratio of D to G bands (I_D/I_G) was combined to
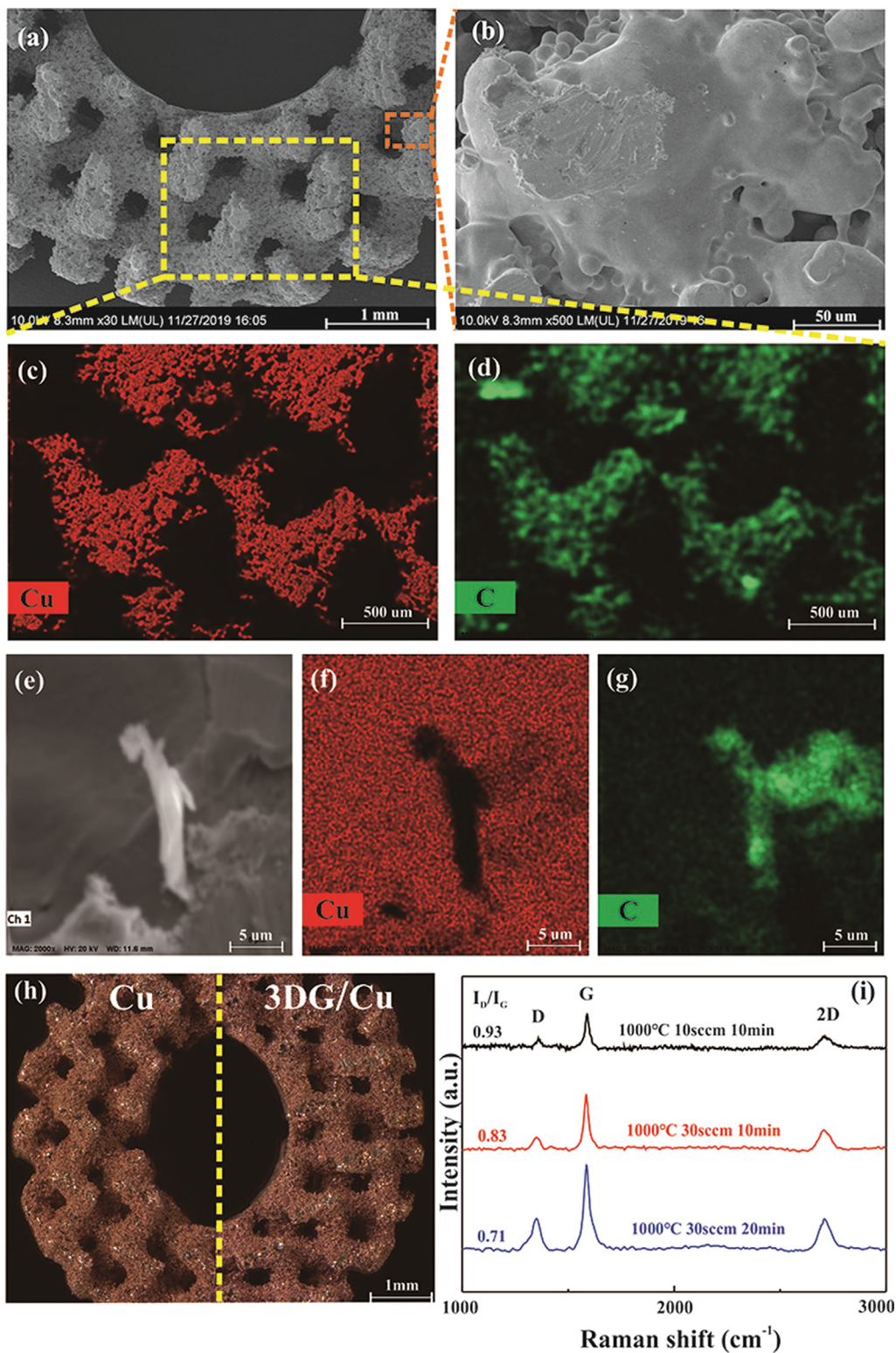
Fig. 8. (a-b) SEM images of 3DG/Cu porous scaffold under different magnifications; EDS mapping image of (c) Cu and (d) C; (e) local magnification of SEM image, corresponding EDS mapping image of (f) Cu and (g) C; (h) comparison before and after graphene growth of OM; (i) Raman spectra of graphene on copper scaffold under different growth conditions. (For interpretation of the references to colour in this figure legend, the reader is referred to the web version of this article.)

reveal the density of defects. With shorter growth times or lower flow rates, the value of I_D/I_G increased from 0.71 to 0.93, indicated an increase of defects mainly attributed to totally disordered imperfect edge structures. As a consequence, an optimal growth condition (growth temperature of 1000 °C, flow rate of CH_4 in 30 sccm, growth time of 20 min) was used for the 3DG/Cu porous structure.

3.4. Thermal property and EMI shielding effectiveness of 3DG/Cu porous scaffolds

Thermal diffusion performance substantially increased upon the addition of graphene on the Cu porous scaffold, up to a 26.8% increase compared to the initial copper reference sample and a 14.8% increase
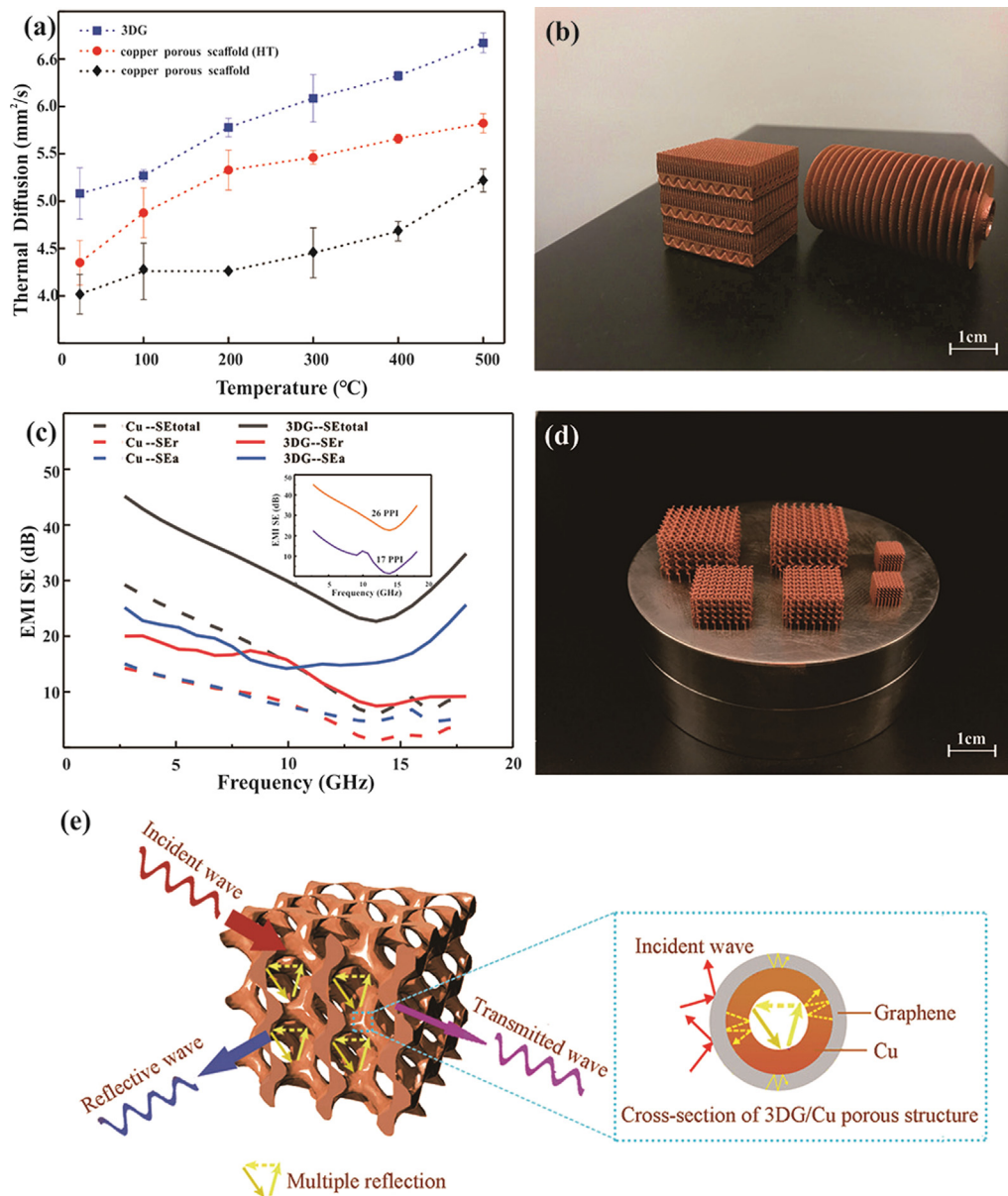
Fig. 9. Performance of 3DG/Cu porous scaffold: (a) thermal diffusion; (b) SLM copper air-liquid crossflow heat exchanger (with micron-scale inner microfluid channel) and a plate-tube structure for thermal management; (c) EMI SE; (d) Copper scaffold with different porosity; (e) Schematic of 3DG/Cu on EMI. (For interpretation of the references to colour in this figure legend, the reader is referred to the web version of this article.)

Table 1
Comparison of the data of graphene-based porous materials with similar composition or structure on EMI shielding performance and thermal performance improvement from literature.

Coating materials	Substrate	Method	Maximum shielding efficiency (dB)	Improvement of thermal property (%)	Ref
Graphene aerogels	Graphite texture	Immersion + freeze dried + anneal + chemical methods	37	–	[50]
Graphene	PS	High-pressure compression molding + salt-leaching	29.3	–	[56]
Graphene	PMMA	Solution blending + melt compounding + batch foaming	19	–	[57]
Cu/Graphene/Cu	Al	Surface modification + electrochemical plating	–	8.5	[58]
Graphene	Ni	Foaming + CVD	–	554	[59]
Graphene	Cu-Ni	Electroless plating + electrophoretic deposition	20	–	[60]
Graphene	Cu	Powder sintering + CVD	–	2.4	[61]
Graphene aerogels	Cu	Freeze-drying + thermal annealing	47	6.3	[62]
Graphene	Cu	CVD + SLM	47.8	27	This work

Note: poly (methyl methacrylate)-PPMA, polystyrene-PS.

to the HT copper samples under the same temperature as the graphene *in-situ* growth (Fig. 9a). Since the special one-atom-thick planar structure of graphene can reduce the barriers for phonon transport, the integration of the 3DG/Cu porous scaffold possesses an enhanced conductance. It is also worth noting that the HT copper sample also obtained a rise in thermal performance due to a grain size growth by 1–2 orders of magnitude during heat treatment. In this case, increased grain size reduces grain boundary scattering which restricts the mean free pathway of heat carrier, thus improving the heat transfer. With respect to the good thermal performance, a sophisticated SLM copper air–liquid crossflow heat exchanger (with inner microfluid channel diameter less than 500 μm) and a plate-tube structure was successfully fabricated (Fig. 9b), further demonstrating its potential for application in complex heat exchangers with advantages of individualization and cost and time-saving. Given the thermal property is close to the materials compositions, the structure of sample, and manufacturing process, we therefore make a rough comparison on the thermal property improvement before and after graphene coating on the metal substrate (Table 1). It could be concluded that this work presented a preferable result compared with similar researches. Other extremely high enhancement mainly resulted from the ultralow thermal conductivity base, like Ni or polymer.

To demonstrate the potential of the 3DG/Cu porous scaffold for EMI, the EMI *SE,* which characterizes the capability to attenuate the electromagnetic (EM) radiation, was investigated over the frequency range of 2–18 GHz (Fig. 9c), exhibiting a slight frequency dependence over the frequency range. With *in-situ* grown graphene on copper porous scaffold, the average *SE* increased from 15.9 to 32.3 dB, with a peak value of 47.8 dB (88.2% increase), far surpassing the commercially required level for application of ~20 dB. The enhanced electrical and thermal properties of 3DG/Cu confirmed a good interface between the graphene and substrate. Ji K et al. [44] proved that EMI of the composites increased with increasing pore density. The EMI *SE* achieved more than 133% improvement with an increased porosity density (i.e., smaller apertures) from 20 to 110 PPI (pores per inch). Rajeev K s group [45] also agreed with this point by adding cenosphere to enhance the porosity of carbon foam in order to optimize the EMI performance. We found similar result by increasing porosity density from 17 to 26 PPI (Fig. 9c insert) and obtained a 105% enhancement in EMI *SE*. In other words, the EMI shielding properties can be adjusted by scaffold porosity with the aid of lightweight design from SLM. The 3DG/Cu porous structure in 26 PPI exhibited an average EMI *SE* of 32.3 dB, corresponding to 99.9% blocking of the EMI waves. The same level of shielding in graphene foam was achieved using a 60 mm thick foam (30 times thicker than our current scaffold) [46]. The EMI shielding performances of 3DG/Cu with similar graphene-based materials are also listed in Tables 1. It could be concluded that the EMI *SE* of the 3DG/Cu in our work is comparable or even higher than those of other 3D graphene-based composites, convincing a relatively promising application potential.

The main mechanisms of EMI consist of reflection (SE_r), absorption (SE_a) and multiple reflections of electromagnetic (EM) waves [47], which are mainly bound up with mobile charge carriers, electric or magnetic dipoles, and interfaces of shielding materials, respectively [48]. Researchers [49] have found that metal like copper with high electrical conductivity, mainly plays a role in reflecting electromagnetic waves, which is attribute to the interaction with free electrons or holes. The graphene is expected to show an absorption dominant EM wave loss resulted from the interaction of the electromagnetic field and electric dipoles [50]. Recent researches on EMI have been exponentially increased. The most commonly used method is to form a three-dimensional conductive network within weak or non-conductive matrix by mixed with metal fillers, such as Cu [51]. For an achievement of better absorption-dominant shielding performance, graphene was generally incorporated into epoxy [52] or SiO_2 [53]. We found that this 3DG/Cu porous scaffold showed an outstanding performance due to the

synergistic shielding mechanisms with a significant increase for both SE_r and SE_a, as schematically shown in Fig. 9e. When the microwaves were incident on the surface of the 3DG/Cu porous scaffold, some waves were immediately reflected into the environment, while the remaining waves penetrated deep inside the porous scaffold. Simultaneously, the bilayer structure of the 3DG/Cu composites provided increased number of interfaces for reflections and absorptions of microwaves owing to the impedance mismatch between layers. The impinging EM waves firstly encountered the graphene layer with the highest charge carrier mobility interaction with the EM waves, resulting in an enhancement of the ohmic loss accounting for the SE_r. On the other hand, the graphene additive alleviated the mismatch impedance between air and copper scaffold, which was greatly beneficial to the EM wave absorption into the scaffold, and as a result, attenuated EM energies by energy dissipation or energy consuming responses. The aforementioned intensive thermal diffusion which helped to convert microwave energy into Joule heating [54]. It is worth to note that the graphene film concurrently enables the microwaves to penetrate the metallic layer longitudinally for further reflection effects. Moreover, the large surface area and porosity of the interconnected graphene network on the gyroid cellular substrate, one of triple periodic minimal surfaces with curved surfaces, facilitated multiple reflections and scattering of EM waves inside the material, thus further promoting the dissipation of EM waves. The scattering of the incident wave especially appeared when it encountered a curved surface [44]. This successive scattering behavior in all directions within the 3D interconnected skeleton highly reduced the radiation intensity until most EM waves were absorbed by the materials. Interestingly, the existing of CVD graphene defects as revealed by Raman spectroscopy and the formation of imperfect substrates as revealed in Section 3.3 also functioned as scattering centers contributing to the enhanced losses caused by dielectric relaxation, thereby realizing a higher shielding performance [55]. It is believed that the EM waves will be trapped by the defect structures, which act as scattering centers to facilitate polarization loss. On the whole, the porous structure of the 3DG/Cu composites can attenuate the radiation by reflection, scattering, and absorption between the graphene film and copper skeleton. The multiple dissipation mechanisms prevented the escape of the microwaves from the scaffold before being absorbed and transformed into heat or other energy.

4. Conclusions

A tunable 3DG/Cu porous scaffold was successfully fabricated with homogenously *in-situ* deposition of graphene layer via CVD method. The anisotropic microstructure and heterogeneous composition were optimized for the copper porous scaffold fabrication. With the accurate design and regulation from composition to structure, the 3DG/Cu structure resulted in a remarkable enhancement in EMI *SE* from an average 15.9 (for reference sample) to 32.3 dB, exhibiting a peak value of 47.8 dB (88.2% increase), as well as a 26.8% increase in the thermal diffusion. The hybrid 3DG/Cu demonstrated extraordinarily synergetic effects in reflection, absorption and multiple reflection shielding mechanisms. These major improvements in EMI and thermal conductivity make the current 3DG/Cu porous scaffolds a promising alternative for applications in EMI shielding and thermal management.

Credit authorship contribution statement

Kaka Cheng: Conceptualization, Methodology, Formal analysis, Writing - original draft. **Wei Xiong:** Validation, Investigation, Writing - original draft. **Yan Li:** Writing - review & editing, Funding acquisition, Resources, Supervision. **Liang Hao:** Funding acquisition. **Chunze Yan:** Resources, Funding acquisition. **Zhaoqing Li:** Validation. **Zhufeng Liu:** Formal analysis. **Yushen Wang:** Investigation, Software. **Khamis Essa:** Writing - review & editing. **Li Lee:** Data curation. **Xin Gong:** Software. **Ton Peijs:** Writing - review & editing, Supervision.

Declaration of Competing Interest

The authors declare that there is no conflict of interest regarding the publication of this paper.

Acknowledgement

Appendix A. Supplementary data

Supplementary data to this article can be found online at https://doi.org/10.1016/j.compositesa.2020.105904.

References

[1] Bai RG, Ninan N, Muthoosamy K, Manickam S. Graphene: a versatile platform for nanotheranostics and tissue engineering. Prog Mater Sci 2018;91:24–69.

[2] Balandin AA, Ghosh S, Bao W, Calizo I, Teweldebrhan D, Miao F, et al. Superior thermal conductivity of single-layer graphene. Nano Lett 2008;8(3):902–7.

[3] Li Y, Zhang H, Crespo M, Porwal H, Picot O, Santagiuliana G, et al. In situ exfoliation of graphene in epoxy resins: a facile strategy to efficient and large scale graphene nanocomposites. ACS Appl Mater Interfaces 2016;8(36):24112–22.

[4] Kang M, Kim J, Jang B, Chae Y, Kim JH, Ahn JH. Graphene-based three-dimensional capacitive touch sensor for wearable electronics. ACS Nano 2017;11(8):7950–7.

[5] Pan Y, Chen M, Hu M, Tian M, Zhang Y, Long D. Probing the room-temperature oxidative desulfurization activity of three-dimensional alkaline graphene aerogel. Appl Catal, B 2020;262:118266–76.

[6] Liao XJ, Ye W, Chen LL, Jiang SH, Wang G, Zhang L, et al. Flexible hdC-G reinforced polyimide composites with high dielectric permittivity. Compos Part A 2017;101:50–8.

[7] Yang HQ, Liu SW, Cao LH, Jiang SH, Hou HQ. Superlithiation of non-conductive polyimide toward high-performance lithium-ion batteries. J Mater Chem A 2018;6(42):21216–24.

[8] Daniels TM, Saithip P, Ditsayut P, Kata J, Kwandara M, Adisorn T, et al. 3D graphene-carbon nanotubes-polydimethyl siloxane flexible electrodes for simultaneous electrochemical detections of Hg. Pb and Cd. Proceedings 2017;1(4):467–70.

[9] Qian L, Lu L. Three dimensional porous graphene-chitosan composites from ice-induced assembly for direct electron transfer and electrocatalysis of glucose oxidase. RSC Adv 2014;4(72):38273–80.

[10] Ding X, HuangY Li SP, Zhang N, Wang JG. 3D architecture reduced graphene oxide-MoS₂ composite: Preparation and excellent electromagnetic wave absorption performance. Compos Part A 2016;90:424–32.

[11] Li XL, Yin XW, Song CQ, Han MK, Xu HL, Duan WY, et al. Self-assembly core–shell graphene-bridged hollow mxenes spheres 3D foam with ultrahigh specific EM absorption performance. Adv Funct Mater 2018. https://doi.org/10.1002/adfm. 201803938.

[12] Lin J, Peng Z, Xiang C, Ruan G, Yan Z, Natelson D, et al. Graphene nanoribbon and nanostructured SnO₂ composite anodes for lithium ion batteries. ACS Nan 2013;7(7):6001–6.

[13] Jiang SH, Agarwal S, Greiner A. Low-density open cellular sponges as functional materials. Angew Chem Int Ed 2017;56:15520–38.

[14] Ito Y, Tanabe Y, Sugawara K, Koshino M, Takahashi T, Tanigaki K, et al. Three-dimensional porous graphene networks expand graphene-based electronic device applications. PCCP 2018;20(9):6024–33.

[15] Sieradzki K, Dimitrov N, Mccall C, Vasiljevic N, Erlebacher J. The dealloying critical potential. J Electrochem Soc 2002;149(8):370–7.

[16] Cao XH, Shi YM, Shi WH, Lu G, Huang X, Yan QY, et al. Preparation of novel 3D graphene networks for supercapacitor applications. Small 2011;7(22):3163–8.

[17] Kashani H, Giroux M, Johnson I, Han J, Wang C, Chen M. Unprecedented electromagnetic interference shielding from three-dimensional bi-continuous nanoporous graphene. Matter 2019;1(4):1077–87.

[18] Song Q, Ye F, Yin X, Li W, Li H, Liu Y, et al. Carbon nanotube-multilayered graphene edge plane core-shell hybrid foams for ultrahigh-performance electromagnetic-interference shielding. Adv Mater 2017;29(31):1701583–90.

[19] Xu X, Guan C, Xu L, Tan YH, Zhang D, Wang Y, et al. Three dimensionally free-formable graphene foam with designed structures for energy and environmental applications. ACS Nano 2019. https://doi.org/10.1021/acsnano.9b08191.

[20] Chen C, Hao Y, Bai X, Ni J, Chung S, Liu F, et al. 3D printed porous Ti6Al4V cage: effects of additive angle on surface properties and biocompatibility; bone ingrowth in beagle tibia model. Mater Des 2019;175:107824–33.

[21] Stašić J, Božić D. The effect of NiB additive on surface morphology and micro-structure of 316L stainless steel single tracks and layers obtained by SLM. Surf Coat Technol 2016;307:407–17.

[22] Ren DC, Zhang HB, Liu YJ, Li SJ, Jin W, Yang R, et al. Microstructure and properties of equiatomic Ti–Ni alloy fabricated by selective laser melting. Mat Sci Eng A-Struct 2020;771:138586–95.

[23] Li X, Cai W, An J, Kim S, Nah J, Yang D, et al. Large-area synthesis of high-quality and uniform graphene films on copper foils. Science 2009;324(5932):1312–4.

[24] Chen ZP, Ren WC, Gao LB, Liu BL, Pei SF, Cheng HM. Three-dimensional flexible and conductive interconnected graphene networks grown by chemical vapour deposition. Nat Mater 2011;10:424–8.

[25] Jadhav SD, Dadbakhsh S, Goossens L, Kruth JP, Humbeeck JV, Vanmeensel K. Influence of selective laser melting process parameters on texture evolution in pure copper. J Mater Process Technol 2019;270:47–58.

[26] Xiong W, Hao L, Li Y, Tang D, Cui Q, Feng Z, et al. Effect of selective laser melting parameters on morphology, microstructure, densification and mechanical properties of supersaturated silver alloy. Mater Des 2019;170:107697–708.

[27] Gu DD, Meiners W, Wissenbach K, Poprawe R. Laser additive manufacturing of metallic components: materials, processes and mechanisms. Int Mater Rev 2013;57(3):133–64.

[28] Liverani E, Toschi S, Ceschini L, Fortunato A. Effect of selective laser melting (SLM) process parameters on microstructure and mechanical properties of 316L austenitic stainless steel. J Mater Process Technol 2017;249:255–63.

[29] Xiang Y, Zhang S, Wei Z, Li J, Wei P, Chen Z, et al. Forming and defect analysis for single track scanning in selective laser melting of Ti6Al4V. Appl Phys A: Mater Sci Process 2018;124:685–98.

[30] Liu Y, Yang Y, Mai S, Di W, Song C. Investigation into spatter behavior during selective laser melting of AlSi316L stainless steel powder. Mater Des 2015;87:797–806.

[31] Leung CLA, Marussi S, Towrie M, Atwood RC, Withers PJ, Lee PD. The effect of powder oxidation on defect formation in laser additive manufacturing. Acta Mater 2019;166:294–305.

[32] Tan X, Kok Y, Toh WQ, Tan YJ, Descoins M, Mangelinck D, et al. Revealing martensitic transformation and α/β interface evolution in electron beam melting three-dimensional-printed Ti-6Al-4V. Sci Rep 2016;6:26039–48.

[33] Kok YH, Tan XP, Loh NH, Tor SB, Chua CK. Geometry dependence of microstructure and microhardness for selective electron beam-melted Ti–6Al–4V parts. Virtual Phys Prototy 2016;11(3):183–91.

[34] Rafi HK, Karthik NV, Gong H, Starr TL, Stucker BE. Microstructures and mechanical properties of ti6al4v parts fabricated by selective laser melting and electron beam melting. J Mater Eng Perform 2013;22(12):3872–83.

[35] Tan X, Kok Y, Tan YJ, Vastola G, Pei QX, Zhang G, et al. An experimental and simulation study on build thickness dependent microstructure for electron beam melted Ti–6Al–4V. J Alloys Compd 2015;646:303–9.

[36] Ramirez DA, Murr LE, Martinez Hernandez, et al. Novel precipitate-microstructural architecture developed in the fabrication of solid copper components by additive manufacturing using electron beam melting. Acta Mater 2011;59(10):4088–99.

[37] Zhou Y, Zeng X, Yang Z, Wu H. Effect of crystallographic textures on thermal anisotropy of selective laser melted Cu-2.4Ni-0.7Si alloy. J Alloys Compd 2018;743:258–61.

[38] Kou S. Welding metallurgy. Second Edition 2003;23:309–48.

[39] Li Gao, Guest Jeffrey R, Guisinger Nathan P. Epitaxial graphene on Cu(111). Nano Lett 2010;10(9):3512–6.

[40] Li XS, Cai WW, Colombo Luigi, Ruoff Rodney S. Evolution of graphene growth on Ni and Cu by carbon isotope labeling. Nano Lett 2009;9(12):4268–72.

[41] Zhang XW, Xu C, Zou ZX, Wu ZH, Yin SQ, Zhang ZL. A scalable polymer-free method for transferring graphene onto arbitrary surfaces. Carbon 2020;161:479–85.

[42] Ferrari AC, Meyer JC, Scardaci V, Casiraghi C, Lazzeri M, Mauri F, et al. Raman spectrum of graphene and graphene layers. Phys Rev Lett 2006;97(18):187401–4.

[43] Zhou SZ, Zhou GY, Jiang SH, Fan PC, Hou HQ. Flexible and refractory tantalum carbide-carbon electrospun nanofibers with high modulus and electric conductivity. Mater Lett 2017;200:97–100.

[44] Ji K, Zhao H, Zhang J, Chen J, Dai Z. Fabrication and electromagnetic interference shielding performance of open-cell foam of a Cu–Ni alloy integrated with CNTs. Appl Surf Sci 2014;311:351–6.

[45] Rajeev K, Mondal DP, Anisha C, Muhamed S, Saroj K. Excellent EMI shielding performance and thermal insulating properties in lightweight, multifunctional carbon-cenosphere composite foams. Compos Part A 2018;12:475–84.

[46] Shen B, Li Y, Zhai W, Zheng W. Compressible graphene-coated polymer foams with ultralow density for adjustable electromagnetic interference (EMI) shielding. ACS Appl Mater Interfaces 2016;8(12):8050–7.

[47] Li N, Huang Y, Du F, He X, Lin X, Gao H, et al. Electromagnetic interference (EMI) shielding of single-walled carbon nanotube epoxy composites. Nano Lett 2006;6(6):1141–5.

[48] Zeng ZH, Chen MJ, Jin H, Li W, Xue X, Zhou LC, et al. Thin and flexible multi-walled carbon nanotube/waterborne polyurethane composites with high-performance electromagnetic interference shielding. Carbon 2016;96:768–77.

[49] Violette Jln WD, Violette MF. Electromagnetic compatibility handbook. New York: Van Nostrand Reinhold Company; 1987.

[50] Song WL, Guan XT, Fan LZ, Cao WQ, Wang CY, Cao MS. Tuning three-dimensional textures with graphene aerogels for ultra-light flexible graphene/texture composites of effective electromagnetic shielding. Carbon 2015;93:151–60.

[51] Wang QL, Xiao SL, Shi Sheldon Q, Xu SY, Cai LP. Self-bonded natural fiber product with high hydrophobic and EMI shielding performance via magnetron sputtering Cu film. Appl Surf Sci 2019;475:947–52.

[52] Li Y, Liu ST, Sun JM, Li S, Chen JL, Zhao Y. Effects of the oxygen content of reduced graphene oxide on the mechanical and electromagnetic interference shielding properties of carbon fiber/reduced graphene oxide-epoxy composites. New Carbon

Mater 2019;34(5):489–98.

[53] Wen B, Cao M, Lu M. Reduced graphene oxides: light-weight and high-efficiency electromagnetic interference shielding at elevated temperatures. Adv Mater 2014;26:3484–9.

[54] Cheng H, Wei S, Ji Y, Zhai J, Zhang X, Chen J, et al. Synergetic effect of Fe_3O_4 nanoparticles and carbon on flexible poly (vinylidence fluoride) based films with higher heat dissipation to improve electromagnetic shielding. Compos Part A 2019;121:139–48.

[55] Wang L, Zhang J, Zhang Q. The effect of MWCNTs on the microwave electromagnetic properties of ferrite–MWCNTs composites. J Mater Sci: Mater Electron 2015;26(3):1895–9.

[56] Ding XY, Peng GR, Huan P, Qiang F, Ming BY, Zhong ML. Efficient electromagnetic interference shielding of lightweight graphene/polystyrene composite. J. Mater Chem 2012;22:18772–4.

[57] Zhang HB, Yan Q, Zheng WG, He ZX, Yu ZZ. Tough graphene-polymer microcellular foams for electromagnetic interference shielding. ACS Appl Mater Interfaces 2011;3:918–24.

[58] Simoncini A, Ucciardello N, Tagliaferri V. Thermal and mechanical improvement of aluminum open-cells foams through electrodeposition of copper and graphene. Manufact Rev 2016. https://doi.org/10.1051/mfreview/2016021.

[59] Pettes MT, Ji H, Ruoff RS, Shi L. Thermal transport in three-dimensional foam architectures of few-layer graphene and ultrathin graphite. Nano Let 2012;12:2959–64.

[60] Ji K, Zhao H, Huang Z, Dai Z. Performance of open-cell foam of Cu–Ni alloy integrated with graphene as a shield against electromagnetic interference. Mater Lett 2017;122:244–7.

[61] Rho H, Lee S, Bae S, Kim TW, Lee DS, Lee HJ, et al. Three-dimensional porous copper-graphene heterostructures with durability and high heat dissipation performance. Sci Rep 2015. https://doi.org/10.1038/srep12710.

[62] Yang XT, Fan SG, Li Y, Guo YQ, Li YG, Ruan KP, et al. Synchronously improved electromagnetic interference shielding and thermal conductivity for epoxy nanocomposites by constructing 3D copper nanowires/thermally annealed graphene aerogel framework. Mat Sci Eng A-Struct 2020. https://doi.org/10.1016/j.compositesa.2019.105670.

[63] Ramirez DA, Murra LE, Martinez E, Hernandez DH, Martinez JL, Machado BI, et al. Novel precipitate-microstructural architecture developed in the fabrication of solid copper components by additive manufacturing using electron beam melting. Acta Mater 2011;59(10):4088–99.

[64] Etris SF, Lieb KC, Sisca VK, Moore IC. The annealability testing of copper. J Test Eval 1973;1(1):10–38.